Operando insights into ammonium-mediated lithium metal stabilization: surface morphology modulation and enhanced SEI development

Journal of Colloid and Interface Science 669 (2024) 699–711

Contents lists available at ScienceDirect

Journal of Colloid And Interface Science

journal homepage: www.elsevier.com/locate/jcis

Regular Article

Operando insights into ammonium-mediated lithium metal stabilization: surface morphology modulation and enhanced SEI development

Giampaolo Lacarbonara [a,*], Matthew Sadd [b], Josef Rizell [b], Luca Bargnesi [a], Aleksandar Matic [b], Catia Arbizzani [a]

[a] Alma Mater Studiorum - University of Bologna, Dept. of Chemistry "Giacomo Ciamician", via Selmi 2, Bologna, Italy
[b] Department of Physics, Chalmers University of Technology, SE, 412 96 Göteborg, Sweden

HIGHLIGHTS

- NH_4PF_6 dual beneficial role, hinders the dendritic growth and accelerate the SEI formation.
- Stable lithium deposition stripping over 1500 cycles.
- Operando confocal Raman spectroscopy demonstrates the electrolyte degradation in forming the SEI.

GRAPHICAL ABSTRACT

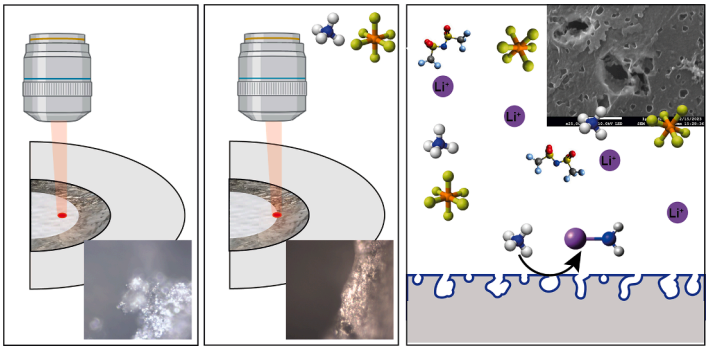

ABSTRACT

Lithium-ion batteries (LiBs) with graphite as an anode and lithiated transition metal oxide as a cathode are approaching their specific energy and power theoretical values. To overcome the limitations of LiBs, lithium metal anode with high specific capacity and low negative redox potential is necessary. However, practical application in rechargeable cells is hindered by uncontrolled lithium deposition manifesting, for instance, as Li dendrite growth which can cause formation of dead Li, short circuits and cell failure.

The electrochemical behaviour of a protic additive (NH_4PF_6) in a carbonate-based electrolyte has been investigated by operando confocal Raman spectroscopy, in situ optical microscopy, and X-ray photoelectron spectroscopy, elucidating its functional mechanism. The ammonium cation promotes a chemical modification of the lithium metal anode-electrolyte interphase by producing an *N*-rich solid electrolyte interphase and chemically modifying the lithium surface morphology by electrochemical pitting. This novel method results in stable lithium deposition and stripping by a decreasing the local current density on the electrode, thus limiting dendritic deposition.

1. Introduction

Because of their high specific energy and power, lithium-ion batteries (LIBs) are the most spread batteries on the market. The employment of graphite and, more recently of silicon/graphite, as anode in LIBs, alleviated the safety concerns that scientists encountered when utilized a Li metal anode in rechargeable batteries [1,2]. However, performance standards have shifted over the past few decades, and the demand for

* Corresponding author.
E-mail address: giampaol.lacarbonar2@unibo.it (G. Lacarbonara).

https://doi.org/10.1016/j.jcis.2024.05.024
Received 20 February 2024; Received in revised form 24 April 2024; Accepted 6 May 2024
Available online 7 May 2024

more specific energy and power has risen, particularly in automotive industry. Li metal anodes appear to be at the cutting-edge once more, and have been proposed for the most modern batteries, especially Gen 4 and Gen 5 [3]. The primary issue of Li-metal anodes is the tendency of non-uniform Li deposition, dendritic and mossy forms, leading to formation of dead Li, continuous electrolyte consumption and large volume changes [4,5].

Without control, the solid electrolyte interphase (SEI) formation inevitably produces morphological and compositional inhomogeneity. Thus, lithium-ion diffusion and deposition follow preferential pathways. Repeated cycling exaggerates this phenomenon, causing lithium deposition in the form of filaments and dendrites. Once dendrites are formed, they become preferential sites for further lithium deposition due to inhomogeneities of the electric field [6].

To counteract problem caused by non-uniform deposition, additives or co-solvents are introduce to the commonly used electrolytes to modify the SEI composition or induce the growth of an artificial SEI. Recently, the electrolyte composition has been varied to enrich the SEI layer with both inorganic compounds, namely LiF, Li_2CO_3, Li_xNO_y or Li_3N, and organic species. Generally, fluorine-containing additives have exceptional reactivity, resulting in a stable SEI due to their dipolar nature [7].

Fluoropyridines (FP) are additives proposed for carbonate and ether-based electrolytes. In these molecules, the C-F bond breaking releases fluoride and enriches the SEI layer with LiF [8,9]. Hence, FP can regulate the initial Li nucleation process and induce a protective layer leading to uniform, dendrite-free, Li deposition. Lithium fluoro(oxalato)borates, additives can also modify the electrode's surface layer composition. These additives produce a LiF-free surface film on the Li-rich cathode, while they produce a LiF-rich surface film on the anode. The presence of LiF in the SEI composition can decrease the diffusion barrier of Li^+, limiting the formation of dendrites [10]. Similarly, hexafluoroisopropyl trifluoromethanesulfonate (HFPTf), heptafluorobutyric anhydride (HFA) and bisfluoroacetamide (BFA) [11,12] can be used to form a uniform LiF-rich SEI, increasing the surface lithophilic character. The homogenous lithium deposition is mainly obtained due to the rapid and uniform Li^+ diffusion through the SEI. Alternatively, phosphorus pentasulfide (P_2S_5) forms a conductive coating on the Li metal anode, suppressing Li dendrite growth during cycling and as well as the shuttle reaction polysulfides in lithium sulphur cells [13].

The molecular structure of the additive must be tailored to reach the desired properties. For example, in phenyl sulfones (PS), the compound's aromatic ring helps to maintain the stability of SEI, and the sulphur moiety ensures high ionic conductivity [14]. On the other hand, the vinyl ethylene carbonate (VEC) structure can solvate Li^+ ions able to permeate through the SEI. The permeability can be controlled using donor solvents. In this system, the properties of the SEI layer formed by the VEC can be modified introducing a cyano-substituent [15].

Several nitrogen-containing species have also shown to form effective SEIs. For this purpose, nitrogen-based interlayers, "artificial SEIs", including lithium phosphorous oxynitride (LiPON) [16] and Li_3N [17] are promising candidates. As an example, Li_3N possesses high ionic conductivity ($\sim 10^{-3}$ S cm^{-1}), low electronic conductivity (less than 10^{-12} S cm^{-1}) [18], and thermodynamic stability versus lithium metal [19,20]. It can be obtained by directly exposing the Li surface to N_2 gas [21].

Also, nitrogen-defective graphite-like carbon nitrides have been studied as coatings to attain homogeneous deposition of lithium metal and block the formation of dendrites [22].

The modification of lithium electrode to produce a high surface area lithium has been proposed by Ryou et al. in 2015, in which idea was to introduce a higher surface area on the Li metal electrode that alleviates high surface area lithium (HSAL) formation and in addition creates "defects by design", that serve as preferred Li plating sites. The physical modification of lithium micro-needle surface structural modification technique took advantage of the ductile nature of lithium and uses roller head containing 20 lines of 200 μm length micro-needle arrays [23,24].

Several studies have focused on understanding interphase dynamics and the strategies to stabilize it. In particular, fundamental studies employed microscopy and dilatometric techniques [22,25–28]. Typically, in situ TEM and SEM [25,29] experiments allow to reach a nanoscale imaging [25,29] with detailed local characterizations of the interphase, but are limited to electrolytes with low volatility and viscosity and it is important to consider the potential influence of the electron beam on the electrochemical reactions. Alternatively, operando ^{7}Li NMR spectroscopy was reported as a promising technique to monitor and recognize different lithium- containing compounds in SEI [30]. Synchrotron X-ray tomographic microscopy has been used to observe the early stage of dendritic lithium formation [31,32] but does not provide chemical information on the SEI. Confocal Raman spectroscopy represents a promising technique for performing operando measurements on batteries over extended number of cycles with a high acquisition speed (<60 s). The spatial resolution depends on the laser spot size. The latter can be regulated and reduced in the order of 1 μm or less depending on the sample. Its applications include materials development, SEI characterization, electrode reaction optimization, and intercalation dynamics, offering real-time (electro)chemical insights. For example, operando Raman spectroscopy, complemented by operando mass spectrometry, was employed to elucidate the mechanism behind SEI formation. identifying major SEI products such as lithium carbonate and lithium oxide [33]. In the study of cathodic materials, in situ and operando Raman spectroscopy aid in understanding M−O bond electrochemistry and lattice dynamics in lithium metal oxides [34]. Raman spectroelectrochemistry was also used to explore Janus graphene's sodium intercalation in sodium-ion batteries [35]. In Li-S cells, with operando Raman spectroscopy, it is possible to track polysulfide speciation and migration, which is vital for enhancing capacity and interphase stability [36].

This work uses operando confocal Raman spectroscopy to study the lithium metal–electrolyte interphase in a carbonate-based electrolyte in the presence of the sacrificial additive NH_4PF_6. The aim is to perform an in situ modification of the lithium surface forming a three dimensional lithium electrode in the early stage of the cycling to reduce the local current density on the lithium surface by electrochemical pitting. This approach is proposed as an innovative strategy to reduce lithium dendritic growth during long-term cycling. The electrochemical behaviour of Li symmetric cells has been explored through galvanostatic cycling and electrochemical impedance spectroscopy, to evaluate the effect of the additive on the electrochemical performance. Confocal Raman spectroscopy was used to probe the variation in the electrolyte composition and the evolution of the interphase during the lithium deposition/stripping experiments.

2. Experimental section

2.1. Materials

The materials used for the preparation of electrodes and electrolytes have been the following: lithium metal ribbon (Sigma Aldrich, 0.75 mm thick, 99,9%), ethylene carbonate (EC, Sigma Aldrich, >99 %), dimethyl carbonate (DMC, Sigma Aldrich, >99), lithium bis(trifluoromethanesulfonyl)imide (LiTFSI, Sigma Aldrich, 99,5%), ammonium hexafluorophosphate (NH_4PF_6, Fluorochem Co., >99 %). The electrolyte solutions to study the effect of NH_4PF_6 as additive for the formation of a stable solid electrolyte interphase have been prepared starting from the electrolyte, 1 M LiTFSI in EC: DMC 1:1 wt./wt., without any additive. The concentrations of the ammonium salt additive are 50, 100 and 250 mM, which are about 1, 2, and 2.5 % wt/wt, respectively, in order. The base electrolyte (1 M LiTFSI in EC: DMC), has been chosen because of its low viscosity (2.88 mPa s^{-1}) in comparison to e.g. the commonly used electrolyte 1 M $LiPF_6$ EC: DMC (4.15 mPa s^{-1}) [37].

2.2. Electrochemical tests

Electrochemical cells with two electrodes have been assembled in a glovebox (Mbraun Labmaster SP) in argon inert atmosphere ($O_2 < 0.1$ ppm and $H_2O < 0.1$ ppm) using stainless steel cells (Swagelok, Swagelok Company) with glass microfiber separators (Whatman, GF/A), which were pre-dried and deaerated in an oven (B-585 Kugelrohr, BÜCHI) at 120 °C under vacuum for 12 h.

The electrochemical tests have been performed with a BioLogic VSP potentiostat/galvanostat. Potentiostatic electrochemical impedance spectroscopy (PEIS) experiments have been conducted in the frequency range 100 kHz – 100 mHz, with a perturbation amplitude of 10 mV around open circuit voltage (OCV) and recording 20 points per decade. The PEIS have been fit using equivalent circuits composed of resistors (R) and constant phase elements (Q). Instead of ideal capacitor, the Q is used to account for nonideal capacitive behaviours originating from a rough and imperfect surface. The impedance of the constant phase element is $Z_{CPE} = 1/[Q(i\omega)^a]$ with Q expressed in $F \bullet s^{-(1-a)}$ (or $\Omega^{-1}\ s^a$) and angular velocity $\omega = 2\pi\nu$. From the fitting results, the capacitance can be obtained as $C = (Q\ R^{1-a})^{1/a}$ [38]. Each (RC) component has its characteristic time constant $\tau = RC$ and it appears in the impedance spectrum at a relative frequency of $\nu = 1/(2\pi\tau)$. The test protocol was the following: EIS (cycle number 0); 10 GCPL cycles at 0.125 mA cm^{-2}; EIS (cycle number 10); 10 GCPL cycles at 0.250 mA cm^{-2}; EIS (cycle number 20); 100 GCPL cycles at 0.500 mA cm^{-2}; EIS (cycle number 120); 10 GCPL cycles at 0.125 mA cm^{-2}; EIS (cycle number 130); prolonged GCPL cycling at 0.125 mA cm^{-2}.

2.3. Confocal Raman spectroscopy measurements

Operando Raman measurements were performed using a two-electrode cell (EL-cell). Lithium foil was cut into a 9 mm disk for the counter electrode that was placed at the bottom of the cell. A 10 mm lithium ring with a 2 mm hole in the centre was used as working electrode, and a 20 mm Cu ring with a 5 mm hole was used as current collector. The assembled cells were connected to a galvanostat/potentiostat Biologic SP-300.

Raman measurements were performed on a LabRAM Confocal Raman Spectrometer with a Peltier cooled CCD, an x50 objective, 300 and 600 grooves/mm gratings, and incident laser 633 nm (power 50 mW 10 % filtered). Before analysis, the spectra were baseline corrected. The laser can be focused close to the lithium-electrolyte interphase in a confocal Raman spectrometer. During the experiments, different areas of the sample were probed with the laser to find a spot close enough to probe the variation in the electrolyte composition and far enough not to focus the laser on the lithium electrode directly. An acceptable compromise was found by focusing the laser ca. 50 μm far from the interphase. Hence, the laser spot was focused in two positions: between the Whatman separator and the working electrode, and ca. 50 μm away from the lithium metal electrolyte interphase. Stripping deposition measurements were made using a Li//Li symmetric cell with the base electrolyte or with the electrolyte containing the additive, by filling the internal volume of the cell with a syringe. Deposition/stripping cycles were carried out with an applied current density of 0.5 mA cm^{-2} or 1 mA cm^{-2} with a capacity of 0.5 or 1 mAh cm^{-2}, respectively.

During deposition stripping cycles, Raman spectra were recorded every 5 min with an exposure time of 60 s by averaging 4 acquisition of 15 s (Fig. 1). The Raman spectra (Fig. S1) were integrated and divided into areas of interest. Table S1 shows the Raman shift ranges used to integrate the electrolyte vibrational band. In situ optical microscopy images were captured before and at the end of the measurements with the x50 objective. During the experiment, fluctuations in room temperature can cause the spectral peaks to shift. A decrease in temperature leads to a blue shift, while an increase in temperature results in a red shift [39]. In the experimental setup used, the maximum observed shift is approximately ± 3 cm^{-1}".

2.4. Physicochemical characterization

Field emission scanning electron microscopy (FE-SEM) was performed by collecting secondary electron signals using a Zeiss (Oberkochen, Germany) SUPRA 40VP instrument at primary beam acceleration voltages of 10–20 kV. Energy dispersive X-ray spectroscopy (EDXS) maps were acquired with an INCA x-act PentaFET Precision spectrometer. Lithium metal electrodes were cycled in the electrolytes under investigation in stainless steel cells (Swagelok, Swagelok Company) with glass microfiber separators (Whatman, GF/A). The cells were disassembled in a glovebox and the lithium metal electrodes placed on SEM stabs in an SEM transfer chamber keeping the argon atmosphere. Pits dimension distribution was obtained by analyzing around 600 pits coming from six different SEM images at different magnification of lithium electrodes by ImageJ software.

X-ray Photoelectron Spectroscopy (XPS) measurements were carried out using a PHI5000 Versa Probe III XPS from ULVAC-PHI, with a monochromatic 1486.6 eV Al Kα X-ray beam. Li electrodes extracted from symmetric Li coin cells after 10 deposition-stripping cycles at 0.5 mA with/without ammonium hexafluorophosphate were compared with Li foils that were soaked in the electrolyte solutions for 20 h, analogous to the cycling time, without any applied potential. Prior to the XPS analysis samples were washed with DMC inside an argon-filled

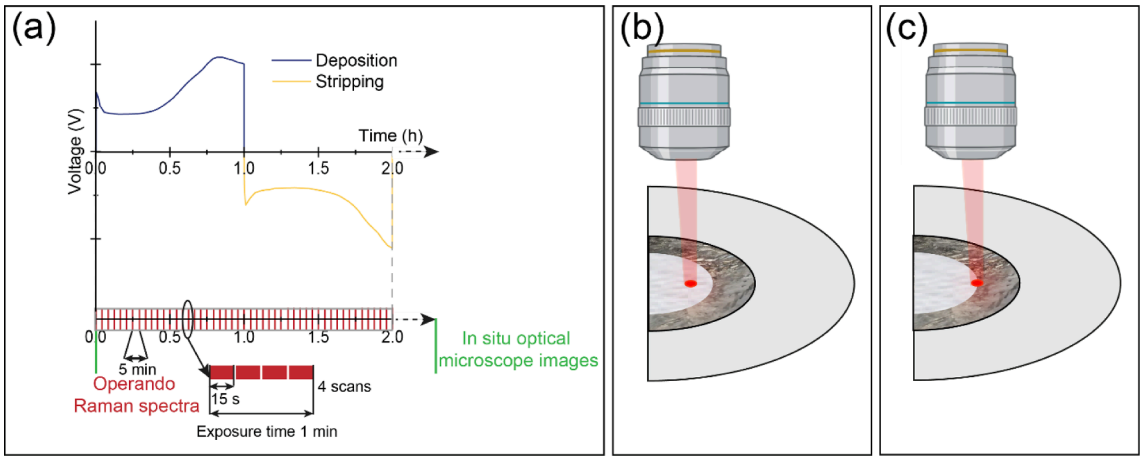

Fig. 1. Schematic representation of the measurement protocol (a) and the sampled areas: ca. 50 μm away from the lithium metal electrolyte interface (b) and between the separator and the working electrode (c).

glovebox before being transferred into the XPS using an air-tight transfer vessel. XPS curves were fitted by the CasaXPS software and applying a Shirley-type background function. The shift in terms of binding energy was corrected assigning a value of 284.1/284.4 eV to the C1s peak attributed to sp2-type carbon. Atomic percentages (at. %) quantification was obtained using the sensitivity factors of integrated peak areas supplied by the software. Each experiment was performed in triplicate (or quintuplicate) to assess the reproducibility.

3. Results

3.1. Electrochemical test

As a protic salt, the action exerted by NH_4PF_6 relies on direct reaction with lithium to modify the chemical composition of the interphase. It has been previously established that the chemical reaction between a protic additive and lithium metal is spontaneous [40]. As shown in the SEM images in Fig. S2, the reaction between lithium metal and ammonium results in chemical pitting on the lithium electrode.

Deposition/stripping cycles and PEIS experiments have been used to investigate the electrolyte behaviour. The voltage profiles of symmetric cells with the two different electrolytes, without and with additive, (Fig. 2) differ in shape and overpotentials. The overvoltage is higher and stable without the additive, showing the typical double peak shape of a Li//Li symmetric cell [41]. Meanwhile, when the additive is present, the overvoltage is initially lower, but increases progressively due to the interphase formation that increases the cell resistance. For the lowest additive concentration, the voltage profile stabilises around 20 mV after five cycles (10 h), suggesting that the formed interphase is stable. This process depends on the current density and the additive concentration, as shown Fig. 2. While the increase of the current density promotes the SEI formation, the increase of the additive concentration results in an increased overvoltage. Higher current densities are likely to promote a faster rate of electrolyte decomposition and thicker SEI formation. Indeed, ammonium ions are forced to shuttle from the electrolyte to the electrode because of migration. This can promote the interaction between the electrolyte and the electrode surface, potentially promoting the decomposition of the electrolyte and the formation of a thick SEI layer. This suggests that the formation of the interlayer is promoted by the presence of the additive through an electrochemically promoted chemical reaction.

Fig. 3 reports on the behaviour of the voltage profile over more than 1500 cycles. With the base electrolyte (1 M LITFSI EC: DMC), the cell exhibits a steadily decreasing overvoltage in, most likely due to the increasing electrode surface area due to dendritic electrodeposition. After 1000 cycles, the overvoltage increases due to the detachment of dendritic lithium and formation of "dead lithium". The formation of the SEI can be related to the increase of the overvoltage observed in the initial cycles (first 50 cycles). With the addition of NH_4PF_6 the overvoltage is stable, and increase with extended cycling is not observed, pointing to a stable interphase.

The interphase properties and formation in the early stages of cycling were investigated by acquiring impedance spectra just after cell assembly, after the cycles at 0.125, 0.250, 0.500 mA cm^{-2} and after 10 cycles at 0.125 mA cm^{-2}, respectively (Fig. 4a, b). The PEIS were fitted with an $R_{el}(R_{SEI}Q_{SEI})(R_{gb}Q_{gb})(R_{ct}Q_{dl})$ equivalent circuit (details of the fitting in Supplementary Information). R_{el} corresponds to the ohmic resistance of the electrolyte, R_{SEI} and Q_{SEI} are related to the SEI impedance, while R_{gb}/Q_{gb} can be ascribed to the grain boundaries inside the SEI and between lithium and SEI. R_{ct}/Q_{dl} are related to the charge transfer process between the liquid electrolyte and lithium electrode across the SEI and the correspondent electrical double layer (Fig. 4c)

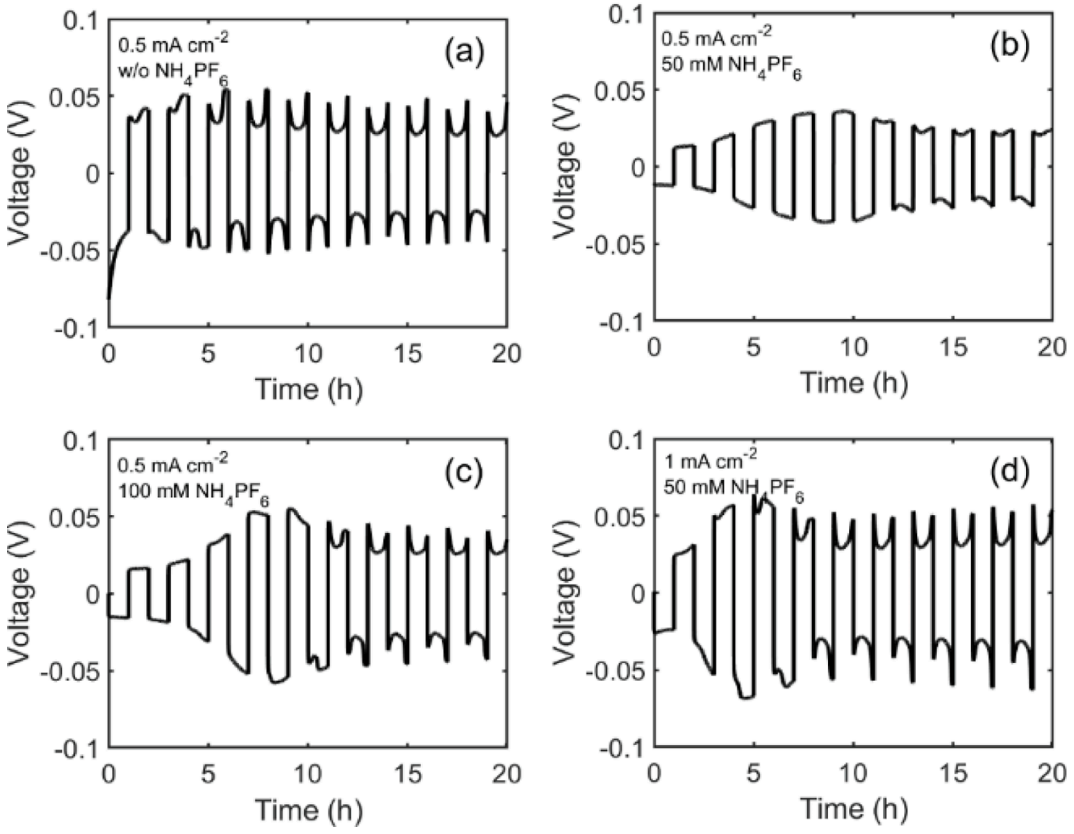

Fig. 2. Deposition-stripping cycles of symmetric Li//Li cells in (a) 1 M LiTFSI EC: DMC, (b) 1 M LiTFSI EC: DMC + 50 mM NH_4PF_6, (c) 1 M LiTFSI EC: DMC + 100 mM NH_4PF_6 at current density of 0.5 mA cm^{-2} and a charge capacity of 0.5 mAh cm^{-2}, and (d) 1 M LiTFSI EC: DMC + 50 mM NH_4PF_6 at current density of 1 mA cm^{-2} and a charge capacity of 1 mAh cm^{-2}.

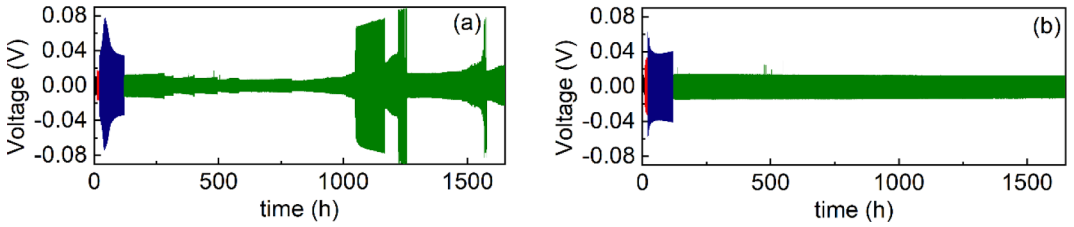

Fig. 3. Li//Li symmetric cell voltage profiles in 1 M LiTFSI EC: DMC (a), and 1 M LiTFSI in EC: DMC + 50 mM NH_4PF_6 in EC: DMC (b), 0.125 mA cm^{-2}, 0.25 mA cm^{-2}, 0.50 mA cm^{-2}.

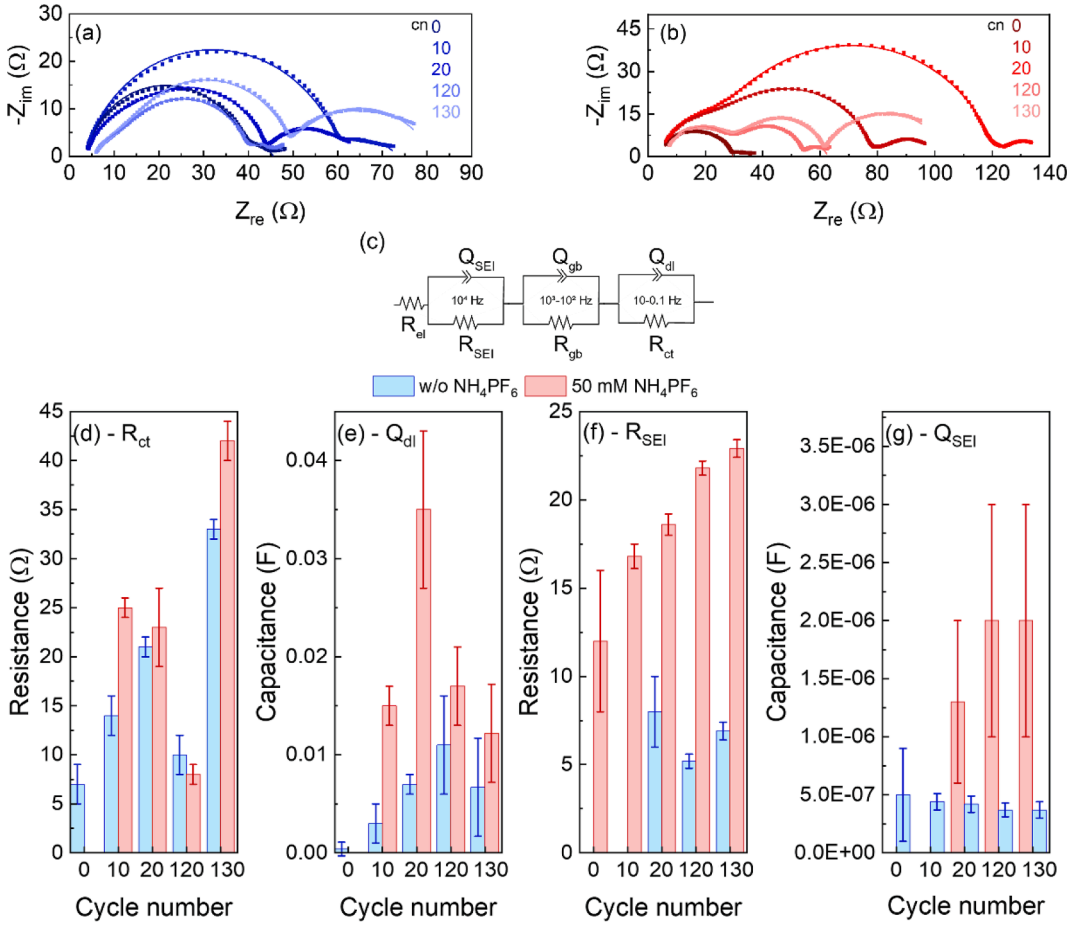

Fig. 4. Li//Li symmetric cell EIS in 1 M LiTFSI EC: DMC (a), and 1 M LiTFSI in EC: DMC + 50 mM NH_4PF_6 in EC: DMC (b) after a different number of cycles at 30 °C. The impedance spectra were fitted with an equivalent circuit $R_{el}(R_{SEI}Q_{SEI})(R_{gb}Q_{gb})(R_{ct}Q_{dl})$. (c) equivalent circuit used to fit the impedance spectra. Evolution of the R_{ct} (d), Q_{dl} (e), R_{SEI} (F), and Q_{SEI} at different cycle numbers with and without NH_4PF_6.

[38]. Each process was assigned by considering the relative frequencies in which they are visible. It must be noted that the representative semicircles of the SEI component are easily recognized thanks to their low capacitive contribution with respect to the double layer of the lithium electrode (10^{-6}F vs 10^{-2}F). Without the additive, the contributions related to the SEI are not easily discerned in the early stage of the measurements, and the contribution given by the bulk and grain boundaries of the SEI are not distinct. On the contrary, these contributions are visible with NH_4PF_6 in agreement with the SEI formation inferred from the voltage profiles.

Looking at the evolution of the impedance components with the cycling, the effect of the ammonium additive can be further compared with the base electrolyte. While adding the ammonium does not drastically alter the charge transfer resistance (Fig. 4d), the capacitance of the double layer increase over the first 20 cycles (Fig. 4e), indicating that NH_4PF_6 leads to an increase in the lithium surface area. In this electrolyte, the capacitance decreases after the cycles at high current density (0.5 mA cm^{-2}), indicating that the high current density cycles did not form a further porous morphology. Contrarily, the decrease in the Q_{dl} suggests that the deposition at 0.5 mA cm^{-2} does not produce dendrites, but rather fill the porosity formed by the electrochemical pitting, with the consequent decrease of the surface area. In both the electrolytes, Q_{SEI} is stable, but it is greater in the lithium electrodes cycled with the NH_4PF_6 due to the higher surface area of these samples. Hence, the addition of NH_4PF_6 causes the increase of the lithium surface area and, hence, the decrease of the local current density for Li deposition, preventing the lithium dendritic growth and stabilizing the SEI.

In the base electrolyte (1 M LiTFSI EC/DMC), the SEI is less resistive with respect to the SEI formed in the presence of the additive. Indeed, if the lithium grows dendritically, freshly-deposited lithium reacts with electrolyte forming a new SEI that is less resistive than the native SEI.

The R_{el} and the components describing the grain boundaries in the

SEI ($R_{gb}Q_{gb}$) seem to not depend on the presence of the additive (Fig. S3). The slight increase of the R_{el} and Q_{gb} can be due to the electrolyte decomposition and the formation of grained structure of SEI, respectively. The PEIS data clearly shows that adding ammonium leads to a fast formation of a stable and porous interphase which is well-developed from the earliest stages of cycling. It is important to understand the composition of the formed interphase and insight about the species present and the evolution of speciation can be obtained by operando Raman spectroscopy.

3.2. Operando Raman spectroscopy

First, the Raman spectra of the electrolytic solutions must be studied to find the region of interest for the operando measurements. The Raman spectra recorded in the operando Raman cell of the electrolytic solutions are shown in Fig. S1a, and all the signals were assigned. The presence of NH_4PF_6 is hard to be detected at this low additive concentration. The only signal present is the one at 732 cm^{-1} associated with the PF_6^- anion [42,43]. For the analysis, two bands were identified with information from all the electrolyte components (Fig. S1b and c).

In situ optical microscopy images of the Li-electrode in the Raman spectroscopy cell before and after cycling show the lithium surface evolution after ten deposition/stripping cycles in the electrolytes without and with additive (Fig. 5).

In the absence of NH_4PF_6 (Fig. 5a and b), significant dendritic growth of lithium can be observed after cycling. This suggests that the density of the freshly deposited Li is lower than the bulk electrode due to the dendritic plating. In the presence of NH_4PF_6, the lithium surface is does not show any dendrites on the micrometre scale probed by optical imaging, as also visible from the enlarged images in the insets (Fig. 5c and d).

Raman spectra were recorded every 5 min during cycling, with a total sample exposure time to the laser of 60 s (Fig. S4). The variation of integrated intensity of representative bands of the electrolyte components during cycling provide information on the variation in the concentration of respective component. (Fig. 6). As shown in Fig. 6a and c, in the absence of NH_4PF_6, the Raman signals fluctuate following the deposition/stripping cycles. The intensity generally decreases during deposition and increase upon stripping. Upon deposition, if dendrites are formed the lithium surface gets closer to the laser spot and the Raman signal related to the electrolyte decreases. After 14 h, the freshly deposited lithium comes into the field of view of the Raman laser; consequently, the electrolyte signals are not yet visible because the deposited lithium cover the whole field of view.

When NH_4PF_6 is present, the Raman signal decreases rapidly in the first reduction, even though the lithium surface is far from the field of view. The EC and the Li^+- EC signals show the most prominent decrease, which can be associated with their reaction at the electrode surface. This suggests that the additive's presence can assist the reaction of the electrolyte component to form the interphase. After the 5th cycle, when the interphase is supposed to be formed, the signals related to the EC and LiTFSI are stable, while the signals of DMC and Li^+-EC increase (zoom in Fig. S5). The latter indicates that once the EC is consumed at the interphase, its concentration in the sampled area is restored by diffusion. However, since the total concentration of EC in solution is lower, it is mostly coordinated with the Li ions and so present as Li^+-EC in the

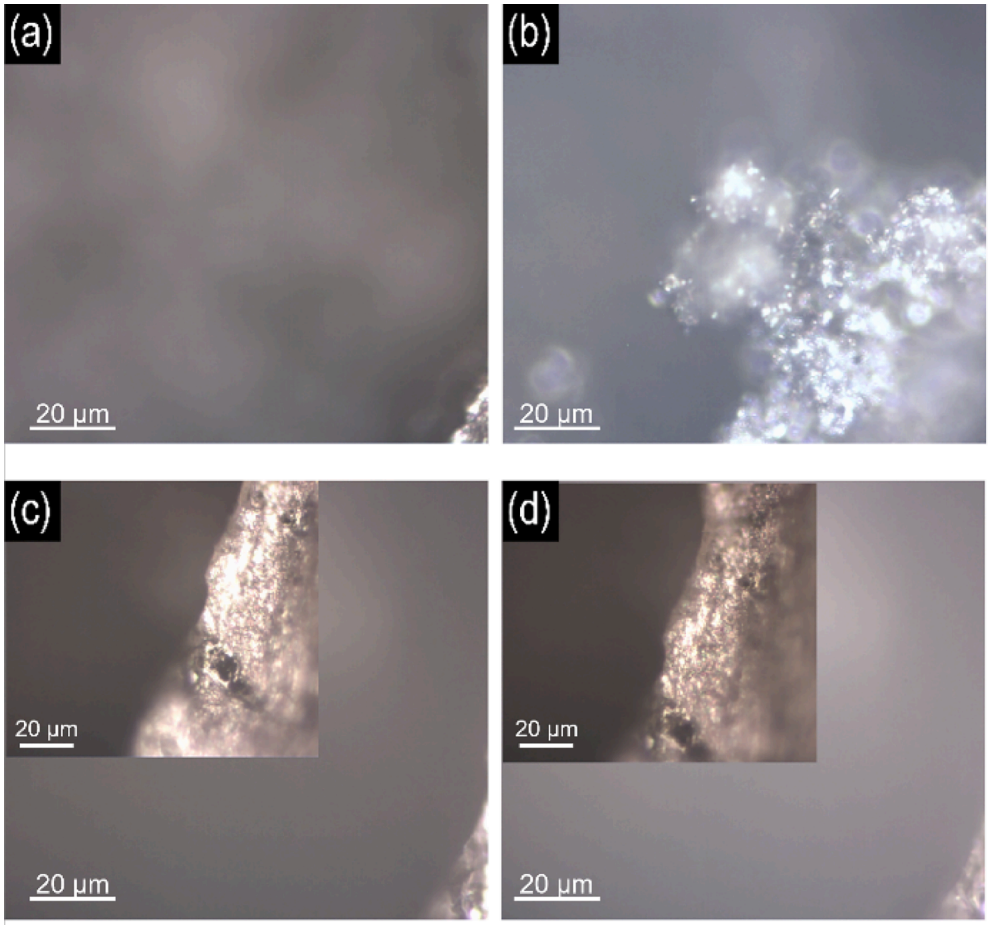

Fig. 5. In situ optical microscopy images (50x) of cell in (a,b) 1 M LiTFSI EC: DMC and (c,d) 1 M LiTFSI EC: DMC + 50 mM NH_4PF_6 before (a,c) and after cycling (b, d) at 0.5 mA cm^{-2}. Lithium surface is in the bottom right corner of the image. The insets of figures (c) and (d) shows the enlargement of the lithium surface that appears in the bottom-right corner.

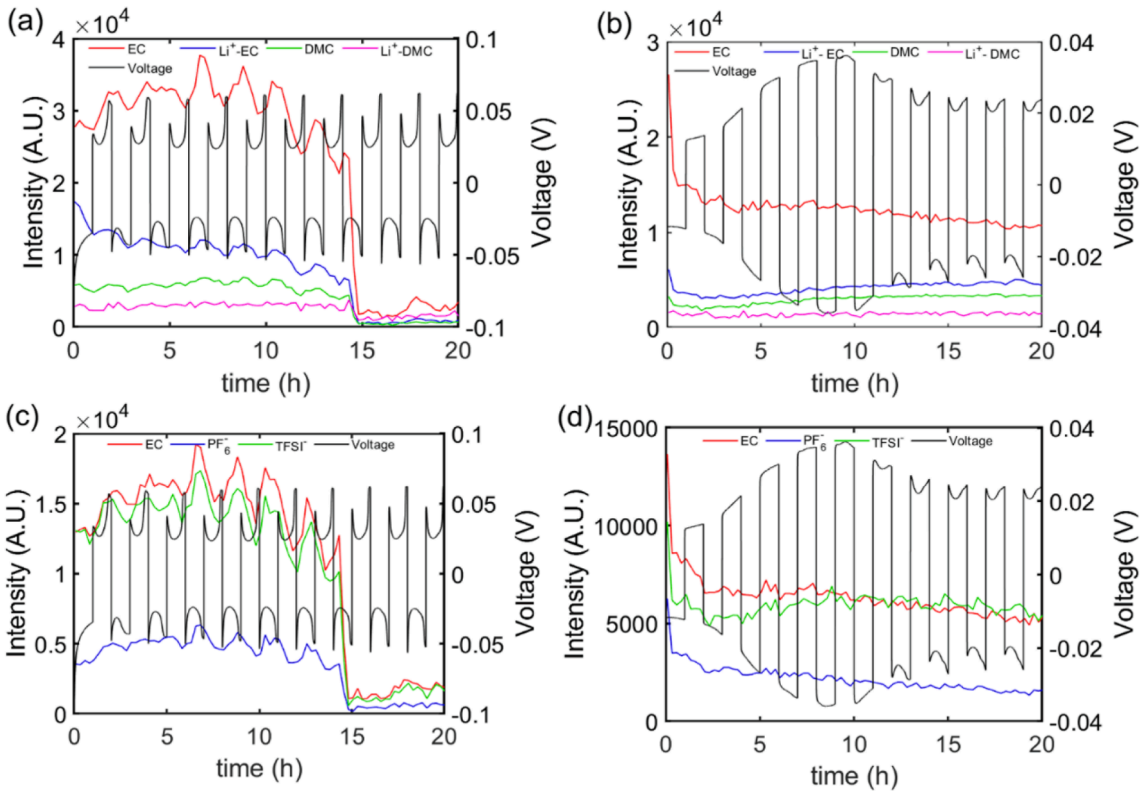

Fig. 6. Operando Raman intensity of selected bands during lithium deposition-stripping in (a,c) 1 M LiTFSI EC: DMC, (b,d) 1 M LiTFSI EC: DMC + 50 mM NH_4PF_6 in the intervals (a,b) 880–945 cm^{-1} and (c,d) 705–725 cm^{-1}. The Li//Li cell with glass fibre separator was cycled at 0.5 mA cm^{-2} for 10 cycles.

Raman spectra.

The Raman laser was also focused on Li surface in the cell with additive. It wasn't possible to perform the same test without additive because of the immediate decrease of all the signals of the electrolyte components. In the Raman spectra become visible a vibration at 1832 cm^{-1} related to lithium carbide that was reported as a degradation product of the SEI under the laser (Fig. S6). Assuming that the decomposed SEI is preserved, or it is every cycle formed in a comparable amount, from the fluctuation of this signal (Fig. 7c) is possible to estimate the reversibility of the lithium deposition stripping (around 85 %). It is also evident the complementarity between the electrolyte signals and the lithium signal that confirms the correlation between the interphase growth and the signal observed (Fig. 7b and c). Once the lithium growth occupies the laser area after 6 h, the electrolyte signals drops while the interphase signals become the only ones visible.

3.3. Morphology and elemental analysis

The morphology of cycled lithium electrodes was studied using SEM. Cells with electrolytes with and without NH_4PF_6 were cycled at a current density of 0.5 $mAcm^{-2}$. After 10 cycles, the cells were disassembled in the glove box and the Li electrodes placed on a SEM holder in the transfer chamber after washing with DMC. The lithium electrode from the cell cycled without the additive shows an inhomogeneous and rough surface (Fig. 8a-c). When the additive is present, the metal electrode surface shows a large number of pits (Fig. 8d and e), with the dimensions ranging from 100 nm to 1 μm. The formation of pits can be ascribed to the reaction of lithium with the ammonium cation. Hence, in the presence of the additive the surface area is increased in the first 10 cycles, lowering the effective current density on the electrode which decreases the driving force for dendritic deposition. While the trend of the surface area in our approach might appear analogous to what is seen with

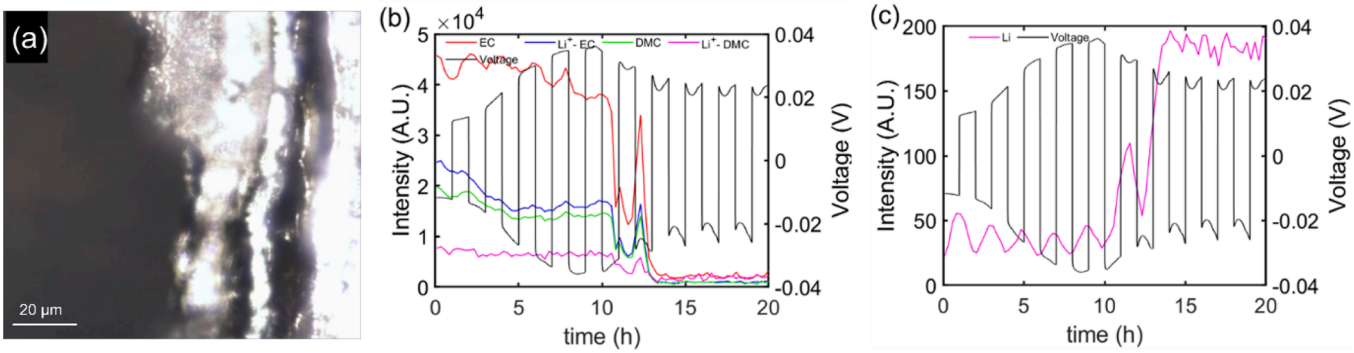

Fig. 7. Experiment recorded focusing the laser at the interface, (a) in situ optical microscopy images (50x) of cell in 1 M LiTFSI EC: DMC + 50 mM NH_4PF_6; operando Raman signals variation during lithium deposition-stripping in1M LiTFSI EC: DMC + 50 mM NH_4PF_6 in the intervals (b) 880–945 cm^{-1} and (c) 1820–1840 cm^{-1}. The Li//Li cell with glass fibre separator was cycled at 0.5 mA cm^{-2} for 10 cycles.

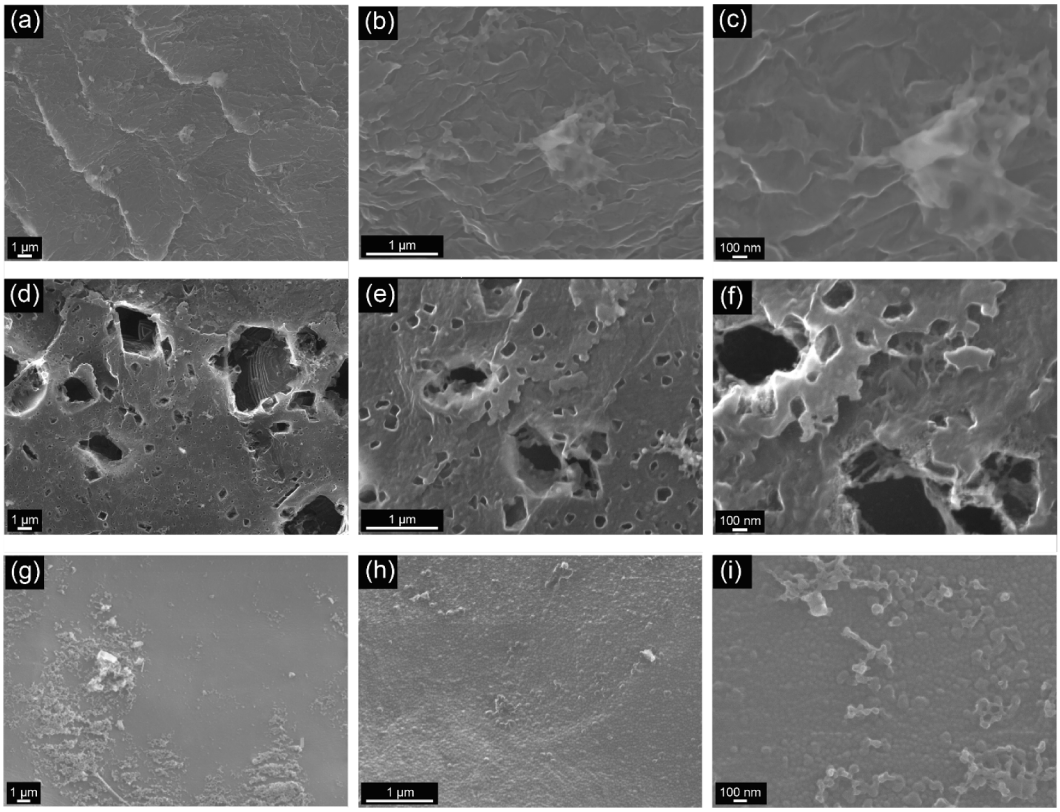

Fig. 8. SEM images of lithium electrodes after 10 deposition/stripping cycles in Li//Li symmetrical cell at 0.5 mA cm^{-2} (0.5 mAh cm^{-2}) and 30 °C in (a-c) 1 M LiTFSI in EC: DMC and (d-f) 1 M LiTFSI in EC: DMC + 50 mM NH_4PF_6. SEM images of lithium electrodes after (g-i) 100 deposition/stripping cycles in Li//Li symmetrical cell 1 M LiTFSI in EC: DMC + 50 mM NH_4PF_6.

dendritic lithium deposition, the impact on lithium morphology is fundamentally different. Dendritic growth is characterized by the formation of needle-like protrusions that can pierce the separator, leading to safety concerns [43]. In contrast, the increased surface area in our system (Fig. 8d and e) arises from the three-dimensional internal structure of the electrode. This intricate architecture provides a larger surface area for lithium deposition without compromising the structural integrity of the separator. After 100 cycles at 0.5 mA cm^{-2} in 1 M LiTFSI in EC: DMC + 50 mM NH_4PF_6, the pits that formed during the early stages of cycling are no longer visible. Instead, the lithium surface appears uniformly flat, with clearly visible lithium nucleation points. Additionally, there are observable nanometric-scale dendritic structures, as shown in Fig. 8i. Huang et al. previously demonstrated that pits or cavities on the lithium surface tend to act as nucleation sites for lithium deposition [44]. Therefore, the pits created by the additive may serve as preferential plating sites, thereby enhancing lithium cyclability, as demonstrated in Fig. 3. This observation aligns with the data from the EIS in Fig. 4e, where a reduction in Q_{dl} after 100 cycles suggests that these pits are being filled with additional lithium deposits.

SEM analyses evidence that the pits are uniformly present on the lithium surface. The pits formed are mostly submicrometric (as can be seen by the size distribution in Fig. 9) with a small fraction of bigger pits that can reach ca. 1 μm (Fig. S9). It must be considered that the chemical pitting, despite less control over the uniformity of the produced pits, can produce a high surface area lithium with pits in the range of 50–200 nm with a very low amount of additive in the electrolytic mixture.

The chemical composition of the electrochemically formed SEI on cycled lithium electrodes was studied by EDS and XPS (Table 1). Electron diffraction mapping was also used to evaluate the element distribution on the electrodes. Elemental maps (Figs. S8–S9) showed the prominent presence of the O, C, N and F on the edge of the pores in samples cycled 1 M LiTFSI in EC: DMC + 50 mM NH_4PF_6. The presence

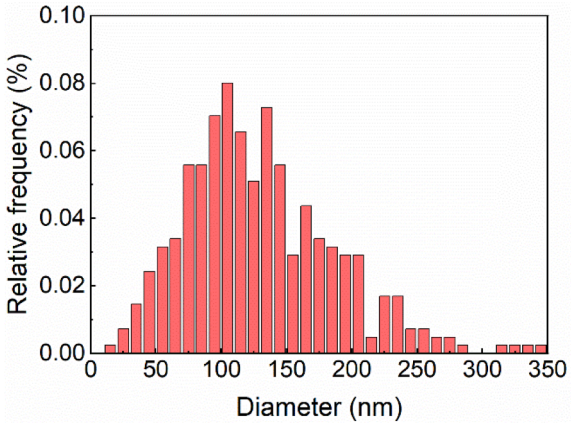

Fig. 9. Pit size distribution histogram in the region 10–350 nm of lithium electrodes after 10 deposition/stripping cycles in Li//Li symmetrical cell at 0.5 mA cm^{-2} (0.5 mAh cm^{-2}) and 30 °C in 1 M LiTFSI in EC: DMC + 50 mM NH_4PF_6.

of Si is related to glass fibre separator residuals on the lithium surface after the cycling. The relative abundance of C, N, F, and S increases in the SEI with the addition of NH_4PF_6, accompanied by a decrease in the relative abundance of O. This suggest that the degradation of the EC and DMC, which are the source of oxygen in the SEI, forms different species in presence of NH_4PF_6. Indeed, the quantity reported are represented as relative percentages. When we consider the degradation of the electrolyte in the system without the additive, the solvents DMC and EC preferentially form O-rich compounds (e.g., carbonates). On the other hand, in the system with NH_4PF_6, oxygen-rich species can be substituted by

Table 1
Chemical composition obtained by EDS, and atomic content obtained by XPS of cycled lithium electrodes, after 10 cycles at 0.5 mA cm^{-2} in a Li//Li symmetric cell in 1 M LiTFSI in EC: DMC with and w/o 50 mM NH_4PF_6, respectively.

Element	w/o NH_4PF_6		50 mM NH_4PF_6	
	EDS	XPS	EDS	XPS
O	58.00	51.69	43.29	36.86
C	28.68	18.32	29.46	30.91
N	3.32	0.94	18.44	3.39
S	0.50	3.11	0.58	7.26
F	9.50	5.88	6.05	17.83
Si	–	20.06	1.93	3.14
P	–	–-	0.58	0.5

nitrogen-enriched species in the SEI (e.g., amides or carbamates). This results in a lower relative oxygen content in the SEI with NH_4PF_6.

The full survey XPS spectra (Fig. S10) of cycled lithium electrodes in the different electrolytes show the characteristic peaks of C1s (284 eV), O1s (532 eV), F1s (689 eV), N1s (400 eV), S2p (170 eV), Li1s (56 eV), P2p (134 eV), and Si2p (155 eV). Atomic percentage quantification is reported in Table S2 and there is an overall qualitative agreement with the results from XPS and EDS. The presence of the additive reduces the number of oxygenated species favouring the formation of S, F and *N*-rich SEI components. It must be noted that all the signals in the XPS spectra were more intense from the lithium electrode cycled in the electrolyte with NH_4PF_6 additive. Hence, the NH_4PF_6 clearly participates in the SEI formation. Indeed, signals in the Li1s, S2p and N1s regions were only visible in the spectrum from the lithium electrode cycled in the presence of the additive even across different electrode spot. The electrode cycled without NH_4PF_6 might have formed a less dense SEI than in presence of NH_4PF_6. Hence, it can be more susceptible to removal during the washing steps involved in sample preparation for XPS analysis. As a result, the XPS probe depth might not reach the underlying lithium metal or nitrogen-containing species within the electrode. Therefore, the absence of Li1s and N1s signals doesn't necessarily imply their complete absence in the electrode. It highlights the importance of considering

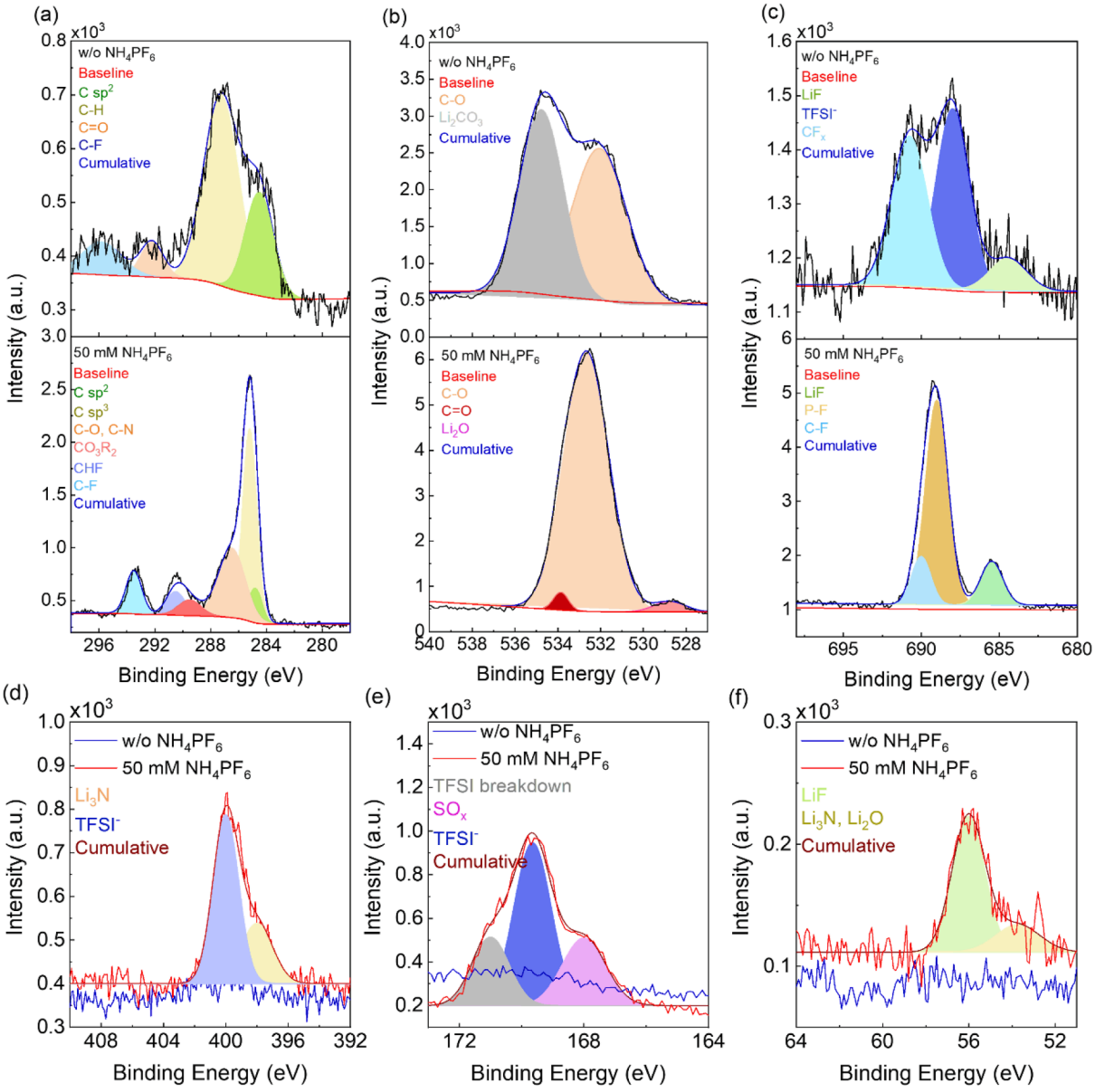

Fig. 10. High-resolution XPS spectra of (a) C1s, (b) O1s, (c) F1s, (d) N1s, (e) S2p, and (f) Li1s regions from cycled lithium electrodes, 10 cycles at 0.5 mA cm^{-2} in Li// Li symmetric cells with 1 M LiTFSI in EC: DMC with and w/o 50 mM NH_4PF_6, respectively.

factors like the removal efficacy of the separator residue and SEI layer characteristics when interpreting XPS data from cycled lithium metal electrodes, especially when the electrolyte composition is altered [45]. However, it must be noted that it is difficult to discriminate if the photoelectron peaks are related to the SEI or to electrolyte residues eventually present after electrode rinsing. A strong washing procedure may also remove SEI components, making the XPS analysis less reliable. A mild washing with DMC is not able to completely remove all the fibers of the separator and sometimes removes not only extraneous salt deposits from the electrolyte but also LiF and Li_xPF_y components of deeper layers of the SEI structure [46].

The highly resolved XPS spectra were fitted to get insights about the influence of the NH_4PF_6 on the SEI. Results of fittings are reported in Table S4 and Fig. 10.

The C 1 s spectrum (Fig. 10a) of the electrode cycled in 1 M LiTFSI (without NH_4PF_6) shows characteristic peaks for C-sp^2 (284.5 eV), C—H (285.2 eV), C═O (292.2 eV), and −C-F (295 eV) [45]. In contrast, the presence of NH_4PF_6 in the electrolyte increases the intensity of unsaturated carbons (C-sp^3 and C—H) and introduces a new peak at 286.8 eV. This peak can be attributed to C—O bonds, but it also overlaps with the typical energy of C—N bonds [47]. Additionally, NH_4PF_6 leads to the presence of carbonate groups (289.2 eV) and CHF (290.5 eV) in the SEI.

The O1s region (Fig. 10b) presents at least two contributions indicating the presence of C═O and carbonates at 532 eV and 534.7 eV, respectively [48]. With the addition of NH_4PF_6 to the electrolyte, C—O is visible at 528.8 eV. Furthermore, a peak at 533.8 eV suggests the formation of Li_2O as a decomposition product of the electrolyte solvent.

Fluorinated components on the lithium surface are evidenced by the F1s spectra (Fig. 10c). Without NH_4PF_6, the TFSI anion signal is visible at 688 eV. Degradation products are present at 688 eV and 685 eV ascribed to the CFx and LiF, respectively, the latter signal is quite intense when NH_4PF_6 is present in the electrolyte [49].

The N1s region (Fig. 10d) is dominated by the TFSI anion photoelectron peak at 400 eV. However, contribution at 398 eV is also observed that could be related to the presence of Li_3N, as a reaction product of the ammonium cation with the lithium metal [50]. A degradation product of the TFSI anion is visible (Fig. 10e) in S2p region as a peak at 168 eV and a shoulder at 171 eV that The former can be ascribed to SO_x, the letter analogous compound to Li_2SO_4 or $LiSO_3CF_3$ that are already been reported as LiTFSI degradation products [51,52]. Signals in the Li1s spectrum (Fig. 10f) are not easy discernible because of the low signal, however two components in the spectra could be identified and can be ascribed to LiF, Li_3N, and Li_2O, accordingly to what observed in the N1s and O1s spectra [53,54]. The P2p spectrum shows a peak at 134.5 eV that is shifted with respect to the photoelectron peak of the PF_6 anion (≈ 136 eV) (Fig. S11). This signal could originate from a reduced compound formed in the reaction between lithium metal and the PF_6 anion [55]. In summary, XPS analysis reveals significant differences in the SEI composition of Li electrodes cycled with and without NH_4PF_6. The presence of NH_4PF_6 promotes the formation of C—O, C—N, and LiF functionalities within the SEI layer, potentially influencing its properties.

4. Discussion

The formation of the solid electrolyte interphase is due to the reaction of the electrolyte at the electrode surface that is promoted by the presence of NH_4PF_6. EIS and SEM evidenced the reactivity of NH_4PF_6, leading to the formation of pits and a high surface area of lithium in the early stage of cycling. In a symmetrical Li cell, the evolution of the interphase depends on both the current density and the additive concentration. With higher current density, the formation of the interphase is favoured, and increasing the NH_4PF_6 concentration increases the overvoltage. This suggests that the additive participates in the development of the interphase in an electrochemically promoted chemical reaction. Long-term cycling with 50 mM of NH_4PF_6 in the electrolyte shows a steady overvoltage profile, which can be attributed to a decreased local current density on the lithium electrode. In the presented system, the chemical pitting of the lithium surface results in a porous morphology of the lithium electrode which is not related to the presence of dendrites. As a result of the new morphology the local current density on the electrode surface is decreased which reduces the formation of dendrites. Similarly to physical modification to increase surface area and create preferred lithium plating sites, NH_4PF_6 addition aimed to achieve a similar effect through a chemical approach. This intricate architecture offers a significantly larger surface area for lithium deposition without compromising the integrity of the separator. SEM analysis confirms the presence of uniformly distributed pits on the lithium surface. These pits are primarily submicrometric in size with a small fraction reaching approximately 1 μm. While this chemical approach offers less control over the uniformity of the pits compared to physical methods, it has the advantage of achieving a high surface area with pits ranging from 50-200 nm by simply adding an additive to the electrolyte. As cycling progresses, the three-dimensional structure of the electrode surface creates multiple preferential sites for lithium nucleation. This, in turn, facilitates uniform lithium deposition, as the deposited lithium fills the pits created earlier, contributing to enhanced lithium cyclability.

This approach is proposed as a suitable strategy to reduce lithium dendritic growth in long-term cycling. The participation of the electrolyte in the interphase formation is confirmed by operando Raman spectroscopy. In the reported experiment, by integrating representative Raman vibrations of electrolyte components, it was possible to follow the variation in the electrolyte concentration by focusing the laser close to the electrode surface. The EC and the LiTFSI: EC electrolyte signals show the most significant drop in the first reduction. This suggests that the additive can assist the reactions of the electrolyte components to form the interphase. In this configuration, in situ optical microscopy also shows an unaltered lithium surface after 10 cycles at 0.5 mA cm^{-2}, while without NH_4PF_6 a clear formation of dendritic lithium was observed.

The chemical composition of the interphase was studied with EDS and XPS spectroscopy. In the presence of NH_4PF_6, electron diffraction maps revealed a six time increase in nitrogen content and the appearance of the phosphorous signal, indicating a participation of the additive in the formation of the SEI, introducing N- and P-groups. This is further confirmed by the presence of stronger signals in the XPS spectra of the lithium electrode cycled in the electrolyte with the NH_4PF_6 additive. Indeed, signals in the Li1s, S2p, P2p and N1s areas were only evident in lithium samples cycled with the additive present. This suggests the formation of thicker SEI in the electrodes cycled with NH_4PF_6. Furthermore, the presence of N- groups was observed as Li_3N in the N1s spectrum and as C—N in the C1s spectrum. Indeed, the high presence of LiF, Li_2O and degradation product of the TFSI and PF_6 anions suggest that the addition of the protic additive promotes the formation of the SEI. This could also be suggested by the carbonate peaks and a more intense C-F peak in the C1s spectra of the lithium cycled in NH_4PF_6 electrolyte. Additionally, the presence of NH_4PF_6 promotes the decomposition of LiTFSI as observed in S2p spectra. In this regard, promoting the formation of the SEI can be beneficial to reduce the number of formation cycles of a cell.

All this information was used to elucidate the mechanism exerted by the NH_4PF_6 (Scheme 1). The proposed mechanism involves the direct reaction of lithium with ammonium by forming lithium amide. This strong basis can react with organic carbonate by nucleophilic substitution forming carbamates which are well known to be plastic and flexibles (e.g., urethanes). Side products such as hydrogen and organic alcohol can enrich the SEI of LiH and lithium organic oxides. These reactions (examples in Scheme 1) produce a nitrogen-enriched SEI.

5. Conclusions

The addition of NH_4PF_6 has a dual beneficial role in terms of

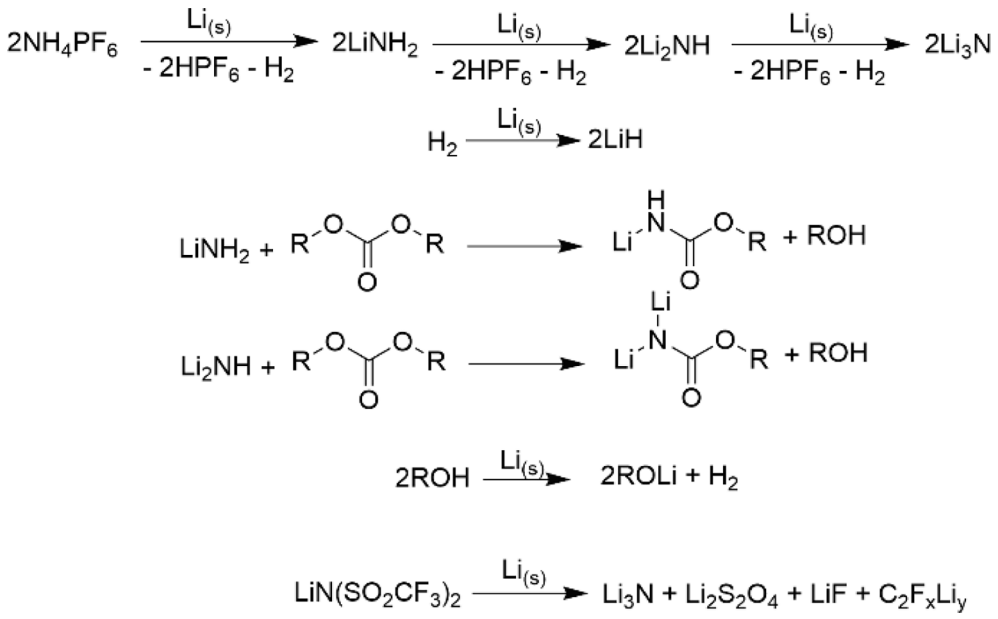

Scheme 1. Proposed reactions involving lithium metal and ammonium hexafluorophosphate.

hindering the dendritic growth and accelerating the formation of the SEI. The key points of ammonium cation action are the chemical modification of the lithium-electrolyte interphase by forming a thicker *N*-rich SEI and the change of the lithium surface morphology to reduce the local current density of the deposition process. The mechanism of action consists of pitting the lithium surface by the protic additive in the first cycles, which lead to a larger surface area. This approach yields stable lithium deposition stripping over 1500 h, because the increased surface area helps in maintaining low the current. SEM confirmed the pitting of lithium electrodes in the first 10 cycles, with pit dimensions in the range of 50–200 nm. The formation of the 3D electrode surface creates numerous preferential sites for lithium nucleation and decreases the electrode's local current density. This, in turn, hinders the dendritic formation as demonstrated by in situ optical microscopy and SEM and contributes to maintain a homogenous current distribution on the electrode surface. The operando confocal Raman spectroscopy demonstrates the role of the additive in the electrolyte degradation in forming the solid electrolyte interphase, and EDS and XPS gave the chemical composition of the obtained interphase. A proposed mechanism involving the direct reaction of lithium with ammonium by forming lithium amide justifies the formation of a high surface area electrode with *N*-rich interphase.

CRediT authorship contribution statement

Giampaolo Lacarbonara: Writing – review & editing, Writing – original draft, Visualization, Supervision, Project administration, Methodology, Investigation, Formal analysis, Data curation, Conceptualization. **Matthew Sadd:** Supervision, Software, Methodology, Formal analysis, Data curation. **Josef Rizell:** Writing – review & editing, Validation, Methodology, Investigation, Formal analysis, Data curation. **Luca Bargnesi:** Writing – review & editing, Visualization, Validation, Investigation, Formal analysis. **Aleksandar Matic:** Writing – review & editing, Visualization, Supervision, Resources, Project administration, Methodology. **Catia Arbizzani:** Writing – review & editing, Writing – original draft, Visualization, Resources, Project administration, Methodology.

Declaration of competing interest

The authors declare that they have no known competing financial interests or personal relationships that could have appeared to influence the work reported in this paper.

Data availability

Data will be made available on request.

Acknowledgements

This research was funded by MiTE (now MASE) ENEA PTR 2022-2024 – Research of Electrical System (RSE) "Development of stable electrodes for Na ion batteries and characterization of the Li anode interphase" as activity of WP1- LA23 "Advanced and sustainable electrolyte and separators for lithium-ion and lithium metal cells" CUP: I53C22003080001. Dr Gioele Pagot and Prof. Vito Di Noto for the kind help in the capturing SEM images in inert atmosphere.

Appendix A. Supplementary data

Supplementary data to this article can be found online at https://doi.org/10.1016/j.jcis.2024.05.024.

References

[1] S. Pain, Power through the Ages Nature 551 (2017) S134–S137, https://doi.org/10.1038/d41586-017-07506-z.
[2] https://ec.europa.eu/eurostat/statistics-explained/index.php?title=Energy_statistics_-_an_overview (last entry 20th February 2024).
[3] Battery 2030+ Roadmap, Inventing the sustainable batteries of the future, Research Needs and Future Actions, updated August 2023, https://battery2030.eu/research/roadmap/.
[4] B. Dunn, H. Kamath, J.M. Tarascon, Electrical energy storage for the grid: a battery of choices, Science 334 (2011) 928–935, https://doi.org/10.1039/C3EE40795K.
[5] W. Xu, J. Wang, F. Ding, X. Chen, E. Nasybulin, Y. Zhang, J.-G. Zhang, Lithium metal anodes for rechargeable batteries, Energy Environ. Sci. 7 (2014) 513–537.
[6] Z. Hong, V. Viswanathan, Phase-Field Simulations of Lithium Dendrite Growth with Open-Source Software, ACS Energy Lett. 3 (7) (2018) 1737, https://doi.org/10.1021/acsenergylett.8b01009.
[7] N. Xu, J. Shi, G. Liu, X. Yang, J. Zheng, Z. Zhang, Y. Yang, Research progress of fluorine-containing electrolyte additives for lithium ion batteries, J. Power Sources Adv. 7 (2021) 100043, https://doi.org/10.1016/j.powera.2020.100043.
[8] Z. Xie, Z. Wu, X. An, X. Yue, A. Yoshida, X. Du, X. Hao, A. Abudula, G. Guan, 2-Fluoropyridine: a novel electrolyte additive for lithium metal batteries with high areal capacity as well as high cycling stability, Chem. Eng. J. 393 (2020) 124789, https://doi.org/10.1016/j.cej.2020.124789.

[9] Z. Xie, X. An, Z. Wu, X. Yue, J. Wang, X. Hao, A. Abudula, G. Guan, Fluoropyridine family: bifunction as electrolyte solvent and additive to achieve dendrites-free lithium metal batteries, J. Mater. Sci. Technol. 74 (2021) 119–127, https://doi.org/10.1016/j.jmst.2020.10.017.
[10] X. Li, J. Liu, J. He, H. Wang, S. Qi, D. Wu, J. Huang, F. Li, W. Hu, J. Ma, Hexafluoroisopropyl trifluoromethanesulfonate-driven easily Li+ desolvated electrolyte to afford Li||NCM811 cells with efficient anode/cathode electrolyte interphases, Adv. Funct. Mater., 31 (2021) 1-9, DOI: 10.1002/adfm.202104395.
[11] J. Huang, J. Liu, J. He, M. Wu, S. Qi, H. Wang, F. Li, J. Ma, Optimizing electrode/electrolyte interphases and li-ion flux/solvation for lithium-metal batteries with qua-functional heptafluorobutyric anhydride, Angew. Chem. Int. Ed. 60 (2021) 20717–20722, https://doi.org/10.1002/anie.202107957.
[12] F. Li, J. He, J. Liu, M. Wu, Y. Hou, H. Wang, S. Qi, Q. Liu, J. Hu, J. Ma, Gradient Solid Electrolyte Interphase and lithium-ion solvation regulated by bisfluoroacetamide for stable lithium metal batteries, Angew. Chem. Int. Ed. 60 (2021) 6600–6608, https://doi.org/10.1002/anie.202013993.
[13] S. Chen, B. Ding, Q. Lin, Y. Shi, B. Hu, Z. Li, H. Dou, X. Zhang, Construction of stable Solid Electrolyte Interphase on lithium anode for long-cycling solid-state lithium–sulfur batteries, J. Electroanal. Chem. 880 (2021) 114874, https://doi.org/10.1016/j.jelechem.2020.114874.
[14] X. Zhang, Q. Wu, X. Guan, F. Cao, C. Li, J. Xu, Lithium dendrite-free and fast-charging for high voltage nickel-rich lithium metal batteries enabled by bifunctional sulfone-containing electrolyte additives, J. Power Sources 452 (2020) 227833, https://doi.org/10.1016/j.jpowsour.2020.227833.
[15] C. Forestier, P. Jankowski, A. Wizner, C. Davoisne, G. Gachot, L. Sannier, S. Grugeon, P. Johansson, M. Armand, S. Laruelle, Comparative investigation of Solid Electrolyte Interphases created by the electrolyte additives vinyl ethylene carbonate and dicyano ketene vinyl ethylene acetal, J. Power Sources 345 (2017) 212–220, https://doi.org/10.1016/j.jpowsour.2017.01.131.
[16] W. Wang, X. Yue, J. Meng, J. Wang, X. Wang, H. Chen, D. Shi, J. Fu, Y. Zhou, J. Chen, Z. Fu, Lithium phosphorus oxynitride as an efficient protective layer on lithium metal anodes for advanced lithium-sulfur batteries, Energy Stor. Mater 18 (2019) 414–422, https://doi.org/10.1016/j.ensm.2018.08.010.
[17] F. Qiu, S. Ren, X. Zhang, P. He, H. Zhou, A high efficiency electrolyte enables robust inorganic–organic solid electrolyte interfaces for fast Li metal anode, Sci. Bull. 66 (9) (2021) 897–903, https://doi.org/10.1016/j.scib.2021.01.007.
[18] Y. Li, Y. Sun, A. Pei, K. Chen, A. Vailionis, Y. Li, G. Zheng, J. Sun, Y. Cui, Robust Pinhole-Free Li3N Solid Electrolyte Grown from Molten Lithium, ACS Cent. Sci. 4 (1) (2018) 97–104, https://doi.org/10.1021/acscentsci.7b00480.
[19] M. Wu, Z. Wen, Y. Liu, X. Wang, L. Huang, Electrochemical Behaviors of a Li3N Modified Li Metal Electrode in Secondary Lithium Batteries, J. Power Sources 196 (19) (2011) 8091–8097, https://doi.org/10.1016/j.jpowsour.2011.05.035.
[20] G. Ma, Z. Wen, M. Wu, C. Shen, Q. Wang, J. Jin, X.A. Wu, Lithium anode protection guided highly-stable lithium-sulfur battery, Chem. Commun. 50 (91) (2014) 14209–14212, https://doi.org/10.1039/c4cc05535g.
[21] M. Dollé, L. Sannier, B. Beaudoin, M. Trentin, J.M. Tarascon, Live scanning electron microscope observations of dendritic growth in lithium/polymer cells, Electrochem. Solid State Lett. 5 (2002) A286–A289, https://doi.org/10.1149/1.1519970.
[22] U.S. Meda, L. Lal, M. Sushantha, P. Garg, Solid Electrolyte Interphase (SEI), a boon or a bane for lithium batteries: A review on the recent advances, J. Energy Storage 47 (2022) 103564, https://doi.org/10.1016/j.est.2021.103564.
[23] M.-H. Ryou, Y.M. Lee, Y. Lee, M. Winter, P. Bieker, Mechanical surface modification of lithium metal: towards improved Li metal anode performance by directed Li plating, Adv. Funct. Mater. 25 (2015) 834–841, https://doi.org/10.1002/adfm.201402953.
[24] H.-S. Bae, I. Phiri, H.S. Kang, Y.M. Lee, M.-H. Ryou, Large-area surface-patterned Li metal anodes fabricated using large, flexible patterning stamps for Li metal secondary batteries, J. Power Sources 514 (2021) 230553, https://doi.org/10.1016/j.jpowsour.2021.230553.
[25] R.L. Sacci, J.M. Black, N. Balke, N.J. Dudney, K.L. More, R.R. Unocic, Nanoscale imaging of fundamental Li battery chemistry: solidelectrolyte interphase formation and preferential growth of lithium metal nanoclusters, Nano Lett. 15 (2015) 2011–2018, https://doi.org/10.1021/nl5048626.
[26] J. Maibach, J. Rizell, A. Matic, N. Mozhzhukhina, Toward operando characterization of interphases in batteries, ACS Materials Lett. 5 (9) (2023) 2431–2444, https://doi.org/10.1021/acsmaterialslett.3c00207.
[27] S. Yang, X. Min, H. Fan, J. Xiao, Y. Liu, R. Mi, X. Wu, Z. Huang, K. Xi, M. Fang, In situ characterization of lithium-metal anodes, J. Mater. Chem. A 10 (2022) 17917–17947, https://doi.org/10.1039/D2TA04309B.
[28] G. Lacarbonara, M. Rahmanipour, J. Belcari, L. Lodi, A. Zucchelli, C. Arbizzani, Dilatometric analysis: a powerful tool for testing and improving cell performance, Electrochim. Acta 375 (2021) 137938, https://doi.org/10.1016/j.electacta.2021.137938.
[29] F. Sagane, R. Shimokawa, H. Sano, H. Sakaebe, Y. Iriyama, In-situ scanning electron microscopy observations of Li plating and stripping reactions at the lithium phosphorus oxynitride glass electrolyte/Cu interface, J. Power Sources 225 (2013) 245–250, https://doi.org/10.1016/j.jpowsour.2012.10.026.
[30] S. Lv, T. Verhallen, A. Vasileiadis, F. Ooms, Y. Xu, Z. Li, Z. Li, M. Wagemaker, Operando monitoring the lithium spatial distribution of lithium metal anodes, Nat. Commun. 9 (2018) 2152, https://doi.org/10.1038/s41467-018-04394-3.
[31] L. Magnier, L. Lecarme, F. Alloin, A. King, R. Bouchet, A. Tengattini, D. Devaux, E. Maire, Tomography imaging of lithium electrodeposits using neutron, synchrotron X-ray, and laboratory X-ray sources: a comparison, Front. Energy Res. 9657712 (2021), https://doi.org/10.3389/fenrg.2021.657712.
[32] M. Sadd, S. Xiong, J.R. Bowen, F. Marone, A. Matic, Investigating microstructure evolution of lithium metal during plating and stripping via operando X-ray tomographic microscopy, Nat. Commun. 14 (2023) 854, https://doi.org/10.1038/s41467-023-36568-z.
[33] N. Gogoi, T. Melin, E.J. Berg, Elucidating the step-wise solid electrolyte interphase formation in lithium-ion batteries with operando raman spectroscopy, Adv. Mater. Interfaces 9 (2022) 2200945, https://doi.org/10.1002/admi.202200945.
[34] E. Miele, W.M. Dose, I. Manyakin, M.H. Frosz, Z. Ruff, M.F.L. De Volder, C.P. Grey, J.J. Baumberg, T.G. Euser, Hollow-core optical fibre sensors for operando Raman spectroscopy investigation of Li-ion battery liquid electrolytes, Nat. Commun. 13 (2022) 165, https://doi.org/10.1038/s41467-022-29330-4.
[35] J. Sun, M. Sadd, P. Edenborg, H. Grönbeck, P.H. Thiesen, Z. Xia, V. Quintano, R. Qiu, A. Matic, V. Palermo, Real-time imaging of Na+ reversible intercalation in "Janus" graphene stacks for battery applications, Sci. Adv. 7 (22) (2021) eabf0812, https://doi.org/10.1126/sciadv.abf0812.
[36] M. Sadd, M. Agostini, S. Xiong, A. Matic, Polysulfide speciation and migration in catholyte lithium−sulfur cells, ChemPhysChem 23 (2022) e202100853.
[37] Y.R. Dougassa, J. Jacquemin, L. El Ouatani, C. Tessier, M. Anouti, Viscosity and carbon dioxide solubility for LiPF6, LiTFSI, and LiFAP in Alkyl carbonates: lithium salt nature and concentration effect, J. Phys. Chem. B 118 (14) (2014) 3973–3980, https://doi.org/10.1021/jp500063c.
[38] M.R. Busche, T. Drossel, T. Leichtweiss, D.A. Weber, M. Falk, M. Schneider, M.-L. Reich, H. Sommer, P. Adelhelm, J. Janek, Dynamic formation of a solid-liquid electrolyte interphase and its consequences for hybrid-battery concepts, Nature Chem 8 (5) (2016) 426–434, https://doi.org/10.1038/nchem.2470.
[39] A. Mestari, R. Gaufrès, P. Huguet, Behaviour of the calibration of a Raman spectrometer with temperature changes, J. Raman Spectrosc. 28 (1997) 785–789, https://doi.org/10.1002/(SICI)1097-4555(199710)28:10<785::AID-JRS148>3.0.CO;2-D.
[40] D. Di Cillo, L. Bargnesi, G. Lacarbonara, C. Arbizzani, Ammonium and Tetraalkylammonium Salts as Additives for Li metal electrodes, Batteries 9 (2) (2023) 142, https://doi.org/10.3390/batteries9020142.
[41] L. Haneke, J.E. Frerichs, A. Heckmann, M.M. Lerner, T. Akbay, T. Ishihara, M. R. Hansen, M. Winter, T. Placke, Editors' Choice—Mechanistic Elucidation of Anion Intercalation into Graphite from Binary-Mixed Highly Concentrated Electrolytes via Complementary 19F MAS NMR and XRD Studies, J. Electrochem. Soc. 167 (2020) 140526, https://doi.org/10.1149/1945-7111/abc437.
[42] Z. Hu, S. Zhang, S. Dong, Q. Li, G. Cui, L. Chen, Self-Stabilized Solid Electrolyte Interface on a Host-Free Li-Metal Anode toward High Areal Capacity and Rate Utilization, Chem. Mater. 30 (12) (2018) 4039–4047, https://doi.org/10.1021/acs.chemmater.8b00722.
[43] C. Naudin, J.L. Bruneel, M. Chami, B. Desbat, J. Grondin, J.C. Lassègues, L. Servant, Characterization of the lithium surface by infrared and Raman spectroscopies, J. Power Sources 124 (2) (2003) 518–552, https://doi.org/10.1016/S0378-7753(03)00798-5.
[44] Y.-K. Huang, R. Pan, D. Rehnlund, Z. Wang, L. Nyholm, First-cycle oxidative generation of lithium nucleation sites stabilizes, Lithium-Metal Electrodes 11 (9) (2021) 2003674, https://doi.org/10.1002/aenm.202003674.
[45] L. Somerville, J. Bareño, P. Jennings, A. McGordon, C. Lyness, I. Bloom, The effect of pre-analysis washing on the surface film of graphite electrodes, Electrochimica Acta 206 (2016) 70–76, https://doi.org/10.1016/j.electacta.2016.04.133.
[46] T. Waldmann, A. Iturrondobeitia, M. Kasper, N. Ghanbari, F. Aguesse, E. Bekaert, L. Daniel, S. Genies, I. Jiménez Gordon, M.W. Löble, E. De Vito, M. Wohlfahrt-Mehrens, Review—post-mortem analysis of aged lithium-ion batteries: disassembly methodology and physico-chemical analysis techniques, J. Electrochem. Soc. 163 (10) (2016) A2149, https://doi.org/10.1149/2.1211609jes.
[47] P. Verma, P. Maire, P. Novák, A review of the features and analyses of the solid electrolyte interphase in Li-ion batteries, Electrochim. Acta 55 (22) (2010) 6332–6341, https://doi.org/10.1016/j.electacta.2010.05.072.
[48] J. Zhang, L. Guo, Q. Meng, W. Wang, Z. Li, M. Chang, M. Liu, Z. Jin, K. Zhao, Polyurethane foam derived nitrogen-enriched porous carbon/reduced graphene oxide composite with sandwich-like nanoarchitectures for supercapacitors, J. Mater. Sci: Mater. Electron. 29 (2018) 9942–9953, https://doi.org/10.1007/s10854-018-9036-x.
[49] V. Nilsson, R. Younesi, D. Brandell, K. Edström, P. Johansson, Critical evaluation of the stability of highly concentrated LiTFSI - Acetonitrile electrolytes vs. graphite, lithium metal and LiFePO4 electrodes, J. Power Sources 384 (2018) 334–341, https://doi.org/10.1016/j.jpowsour.2018.03.019.
[50] Q. Wang, Z. Yao, C. Zhao, et al., Interface chemistry of an amide electrolyte for highly reversible lithium metal batteries, Nat. Commun. 11 (2020) 4188, https://doi.org/10.1038/s41467-020-17976-x.
[51] C. Xu, B. Sun, T. Gustafsson, K. Edström, D. Brandell, M. Hahlina, Interface layer formation in solid polymer electrolyte lithium batteries: an XPS study, J. Mater. Chem. A 2 (2014) 7256–7264, https://doi.org/10.1039/C4TA00214H.
[52] K. Forster-Tonigold, F. Buchner, J. Bansmann, R.J. Behm, A. Groß, A Combined XPS and Computational Study of the Chemical Reduction of BMP-TFSI by Lithium, Batteries & Supercaps 5 (2022) e202200307.
[53] I. Ismail, A. Noda, A. Nishimoto, M. Watanabe, XPS study of lithium surface after contact with lithium-salt doped polymer electrolytes, Electrochimica Acta 46 (10–11) (2001) 1595–1603, https://doi.org/10.1016/S0013-4686(00)00758-1.
[54] C. Yan, Y.-X. Yao, X. Chen, X.-B. Cheng, X.-Q. Zhang, J.-Q. Huang, Q. Zhang, Lithium Nitrate Solvation Chemistry in Carbonate Electrolyte Sustains High-Voltage Lithium Metal Batteries, Angew. Chem. Int. Ed. 57 (2018) 14055, https://doi.org/10.1002/anie.201807034.
[55] A.M. Andersson, M. Herstedt, A.G. Bishop, K. Edström, The influence of lithium salt on the interfacial reactions controlling the thermal stability of graphite anodes,

Electrochim. Acta 47 (12) (2002) 1885–1898, https://doi.org/10.1016/S0013-4686(02)00044-0.